Nonlinear light scattering in molecules triggered by an impulsive x-ray Raman process

Konstantin E. Dorfman,[*] Kochise Bennett,[†] Yu Zhang, and Shaul Mukamel[‡]

University of California, Irvine, California 92697-2025, USA

The time- and frequency-resolved nonlinear light scattering (NLS) signals from a time-evolving charge distribution of valence electrons prepared by impulsive x-ray pulses are calculated using a superoperator Green's function formalism. The signal consists of a coherent $\sim N^2$-scaling difference-frequency-generation and an incoherent fluorescence $\sim N$-scaling component, where N is the number of active molecules. The former is given by the classical Larmor formula based on the time-dependent charge density. The latter carries additional information about the electronic structure and may be recast in terms of transition amplitudes representing quantum matter pathways.

PACS number(s): 42.50.−p, 42.55.Vc, 33.20.Fb

I. INTRODUCTION

Newly developed attosecond x-ray sources can excite molecular electronic states impulsively, paving the way for novel spectroscopic probes of electronic structure and correlations [1–10]. Thanks to their broad bandwidth, such pulses can prepare molecules or molecular ions in nonstationary superpositions of electronic states [11]. These states can be probed by various nonlinear optical techniques, such as photoelectron spectroscopy [12,13].

Traditional x-ray experiments [14], including x-ray absorption near-edge structure (XANES), resonant and nonresonant x-ray emission spectroscopy (RXES and NXES), Auger electron spectroscopy (AES), and x-ray diffraction [15] (XD), are mostly related to single-particle characteristics of the many-body ground-state wave-function. Quantum coherence (i.e., the phase in a superposition of states), which is accessible by nonlinear spectroscopy, does not play a role in these techniques. Coherent x-ray sources can look into these quantum effects. In particular, the large bandwidth (10 eV for an 100 as pulse) can be used to create electronic coherences which provide a higher level of information about orbitals that goes beyond the charge density [16]. Nonlinear effects in the x-ray regime have long been observed in the frequency domain [17], including parametric down conversion [18–20], hard x-ray frequency doubling [21], and two-photon x-ray fluorescence [22]. Combined optical plus x-ray nonlinear techniques can monitor excitations of optically excited states [18,23,24]. All–x-ray nonlinearities such as pump-probe have been demonstrated as well [11,19–21,25–27].

Classically, spontaneous emission is related to the acceleration of charges [13]. In the semiclassical approach (classical field and quantum matter) [28] the emission spectrum is thus calculated from a time-dependent charge density that acts as a source. No other information about the matter is needed. This results in the Larmor formula for the power emitted by a radiating charge [Eq. (15)] [13,29]. In a more rigorous description where both field and matter are treated quantum mechanically [30], we must work in the joint field-matter space

and calculate the signal perturbatively in the radiation-matter coupling. Radiation backreaction is then included implicitly through the joint dynamics of field and matter.

In the present work we study the nonlinear light scattering (NLS) caused by the time-evolving superposition of electronic excitations. In order to create such superpositions, the coherent x-ray source with broad (~ 10 eV) bandwidth is required. We use the many-body Green's function formalism [31] to calculate NLS involving two transitions between valence excitations triggered by the stimulated x-ray Raman process [10,32,33] (see Fig. 1). Note that NLS results from the single pulse used for excitation; there is no probe pulse to stimulate the emission. The resulting time- and/or frequency-gated signals [34,35] provide direct information on valence electron motions, coherences, and correlations [10,36]. We identify two possible mechanisms for this process to quadratic order in x-ray pulse intensity: difference-frequency-generation (DFG) and stimulated-Raman-induced fluorescence (SRIF). The former is a coherent process associated with long-range valence-state coherence, which can be described in terms of the time-dependent charge density created by the Raman process, i.e., the classical Larmor formula. It is highly directional (phase matched) and scales as $N(N-1)$ with the number of active molecules. The latter is an incoherent process coming from excited-state populations, which requires more detailed information about the excited states than the simple charge density. It produces an isotropic signal and scales as N. For small samples, the coherent process is dominated by a short-range coherence coming from the neighbor molecules that gives rise to an isotropic emission and scales linearly with N. We compare these two contributions amino acid cysteine excited at the S, O, and N core transitions.

The paper is organized as follows. In Sec. II we present general formal expressions for the coherent and incoherent signals that allow us to incorporate an arbitrary sequence of preparation pulses. The coherent signal is given by the time-dependent polarization, whereas the incoherent signal is expressed in terms of a transition amplitude. In Sec. III we skip the preparation stage (the shaded area in Fig. 2). Assume that the system has been prepared in a superposition state and calculate the spontaneous light emission. In Sec. IV we apply the results of Sec. III to compute the spectra of cysteine induced by a stimulated x-ray Raman process. We further show that

―――――

[*]kdorfman@uci.edu

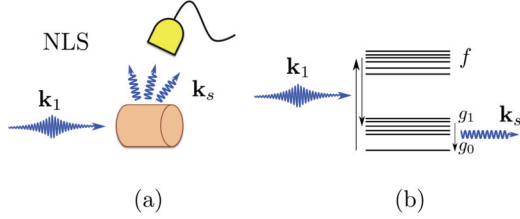[†]kcbennet@uci.edu

[‡]smukamel@uci.edu

FIG. 1. (Color online) (a) Setup for the x-ray–induced NLS and (b) level scheme of the model system, where g_0,..., g_1 represent valence states and f are core excited states.

when the preparation is included as in Sec. II the coherent and incoherent signals represent difference-frequency-generation and fluorescence, respectively.

II. COHERENT VS INCOHERENT SPONTANEOUS LIGHT-SCATTERING SIGNALS

Time- and frequency-gated spontaneous light emission signals are given by an integrated intensity of the electric field of the emitted photons. It may be represented by the spectral and temporal overlap of a bare signal W_B and a detector spectrogram W_D [34]:

$$S(\bar{t},\bar{\omega}) = \int_{-\infty}^{\infty} dt' \frac{d\omega'}{2\pi} W_D(\bar{t},\bar{\omega}; t',\omega') W_B(t',\omega'). \quad (1)$$

The detector offers a window of observation centered at time $\bar{t}$ and frequency $\bar{\omega}$. Even though $\bar{t}$ and $\bar{\omega}$ can be varied independently, the actual temporal σ_T and spectral σ_ω resolutions are not independent and satisfy $\sigma_T \sigma_\omega \geqslant 1$. This is guaranteed by Eq. (1). We shall assume a point-size detector, therefore omitting all effects of spatial resolution, retaining only temporal and spectral gating [34]. Equation (1) was introduced originally as signal processing for the classical field [35], but it more broadly applies to quantum fields as well [34]. The bare signal W_B contains all of the relevant information about the externally driven molecules and is given by a correlation function of matter that further includes a sum over the detected modes. In Appendix A we present superoperator expressions for W_B of a system prepared in an arbitrary
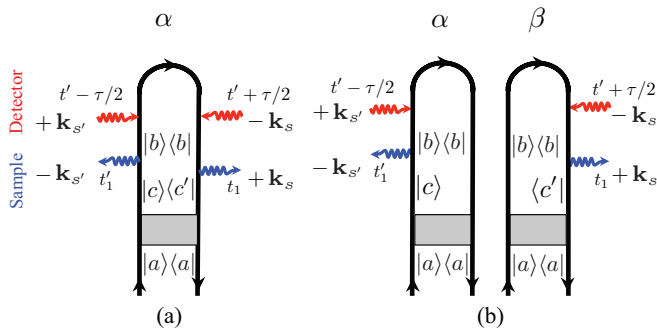

FIG. 2. (Color online) (a) Loop diagram for the bare incoherent signal in a gated measurement caused by a single molecule α, and (b) coherent signal generated by a pair of molecules $\alpha \neq \beta$. Equations (2) and (3) (coherent) and Eqs. (8) and (9) (incoherent) can be read off these diagrams (for diagram rules see Ref. [37]). The shaded area represents an excitation by an arbitrary sequence of pulses, which prepares the molecule in a superposition state.

nonstationary state without treating the preparation explicitly. The bare signal (A6) represented by the closed-path time-loop diagram shown in Figs. 2(a) and 2(b) is given by time-ordered Green's functions for superoperators (TIGERS) [31]. It contains a double summation over molecular positions $\mathbf{r}_\alpha$ and $\mathbf{r}_\beta$ and contains two types of contributions: incoherent emission terms with $\alpha = \beta$ [Fig. 2(a)] and coherent emission $\alpha \neq \beta$ [Fig. 2(b)].

We start with the coherent emission which is induced by pairs of molecules labeled α and β. Here we can factorize the matter correlation in Eq. (A6) $\langle \mathcal{T} \hat{V}_L^\alpha(t_1') \hat{V}_R^{\beta\dagger}(t_1) \rangle \rightarrow \langle \hat{V}_L^\alpha(t_1') \rangle \langle \hat{V}_R^{\beta\dagger}(t_1) \rangle$. W_B is then factorized into a product of amplitudes (see Appendices B and C):

$$W_{B\text{coh}}(t',\omega')$$
$$= A^2 \sum_\mu \int_0^\infty d\tau e^{-i\omega'\tau} \sum_{\alpha=1}^{N} \sum_{\beta=1}^{N-1} \frac{e^{i\mathbf{k}_n \cdot (\mathbf{R}_\beta - \mathbf{R}_\alpha)}}{R_\alpha R_\beta} \ddot{P}^{(\alpha,\mu)}$$
$$\times (t' - \tau/2 - R_\alpha/c) \ddot{P}^{(\beta,\mu)*}(t' + \tau/2 - R_\beta/c). \quad (2)$$

The polarization of molecule α in the Cartesian direction μ is given by

$$P^{(\alpha,\mu)}(t)$$
$$= \sum_{a,b} \rho_{aa} \left\langle \langle bb | \mathcal{T} V_{\mu L}(t) \exp\left(-\frac{i}{\hbar} \int_{-\infty}^{t} H_-'(T) dT \right) | aa \rangle \right\rangle_\alpha, \quad (3)$$

where ρ_{aa} represents the initial equilibrium density matrix, and $\mathcal{T}$ is responsible for time ordering of superoperators. When using a purely temporal gate, $F_f(\omega,\bar{\omega}) = 1$ and we get $W_D(\bar{\omega},\bar{t};t,\tau) = \delta(\tau) F_t^*(t + \tau/2,\bar{t}) F_t(t - \tau/2,\bar{t})$, where $W_D(\bar{\omega},\bar{t};t,\tau) = \int_{-\infty}^{\infty} \frac{d\omega}{2\pi} e^{i\omega\tau} W_D(\bar{\omega},\bar{t};t,\omega)$. For an ideal time gate, $|F_t(t,\bar{t})|^2 = \delta(t - \bar{t})$ and Eqs. (1) and (2) result in the time-resolved signal

$$S(\bar{t}) = |E(\bar{t})|^2, \quad (4)$$

i.e.,

$$S_{\text{coh}}(\bar{t}) = A^2 \sum_\mu \left| \sum_{\alpha=1}^{N} \frac{e^{-i\mathbf{k}_n \cdot \mathbf{R}_\alpha}}{R_\alpha} \ddot{P}^{(\alpha,\mu)}(\bar{t} - R_\alpha/c) \right|^2, \quad (5)$$

where A is a normalization constant and the double dot represents the second time derivative. In the opposite, pure frequency gating, i.e., $F_t(t,\bar{t}) = 1$, and the frequency gate is very narrow, such that $F_f(t,\bar{\omega}) = \frac{\sqrt{\gamma}}{\pi} e^{-i\bar{\omega}t - \gamma t}\theta(t)$ at $\gamma \rightarrow 0$, then $W_D(\bar{\omega},\bar{t};\omega,\tau) = e^{-i\bar{\omega}\tau}$. We then obtain the frequency-resolved signal

$$S(\bar{\omega}) = |E(\bar{\omega})|^2, \quad (6)$$

where $E(\omega) = \int_{-\infty}^{\infty} dt E(t) e^{i\omega t}$. Using Eq. (2) we obtain

$$S_{\text{coh}}(\bar{\omega}) = A^2 \sum_\mu \left| \sum_{\alpha=1}^{N} \frac{e^{i(\bar{\omega}R_\alpha/c - \mathbf{k}_n \cdot \mathbf{R}_\alpha)}}{R_\alpha} \bar{\omega}^2 P^{(\alpha,\mu)}(\bar{\omega}) \right|^2. \quad (7)$$

It follows from the Larmor formula Eqs. (5) or (7) that only when the measurement is either solely time- or frequency-gated can the coherent signal be expressed in terms of the modulus square of a matter amplitude. The more general

time- and frequency-gated signals (A1), (A6), and (2) do not have this form.

We next turn to the incoherent signal [Fig. 2(a)] originating from processes in which both signal-mode interactions occur with the same molecule $\alpha = \beta$. This signal is not given by a modulus square of the polarization amplitude. However, by expanding it in the molecular eigenstates we can express it in terms of other types of amplitudes. After a bit of algebra (see Appendix C for details) we obtain

$$W_{B\text{inc}}(t',\omega') = A^2 \sum_{\mu} \int_0^{\infty} d\tau \, e^{-i\omega'\tau} \sum_{\alpha=1}^{N} \frac{1}{R_\alpha^2} \sum_{a,b} \rho_{aa} \ddot{T}_{ba}^{(\alpha,\mu)}$$
$$\times (t' - \tau/2 - R_\alpha/c) \ddot{T}_{ab}^{(\alpha,\mu)*}(t' + \tau/2 - R_\alpha/c). \tag{8}$$

Here

$$T_{ba}^{(\alpha,\mu)}(t) = \langle b(t)| \mathcal{T} V_\mu(t) \exp\left(-\frac{i}{\hbar} \int_{-\infty}^t H'(T) dT\right) |a\rangle_\alpha \tag{9}$$

represents a matter transition amplitude of molecule α starting with the initial state a and reaching the final state b at time t.

For a pure time domain gating (4), Eq. (8) gives

$$S_{\text{inc}}(\bar{t}) = A^2 \sum_{\mu,a,b} \sum_{\alpha=1}^{N} \frac{1}{R_\alpha^2} \left| \ddot{T}_{ba}^{(\alpha,\mu)}(\bar{t} - R_\alpha/c) \right|^2. \tag{10}$$

Pure frequency gating (6) yields

$$S_{\text{inc}}(\bar{\omega}) = A^2 \sum_{\mu,a,b} \sum_{\alpha=1}^{N} \frac{1}{R_\alpha^2} \bar{\omega}^4 \left| T_{ba}^{(\alpha,\mu)}(\bar{\omega}) \right|^2. \tag{11}$$

Equations (8)–(11) indicate that the incoherent signal may not be generally recast in the form of a square of the total polarization alone [Eq. (3)]. Rather, it depends on a different set of matter quantities-transition amplitudes (9) that represent the possible quantum pathways of matter from state a to state b. This calculation does not require superoperators, since the amplitudes represent the evolution of the bra or ket separately and can be recast in Hilbert space. The polarization (3), on the other hand, is governed by evolution of both bra and ket and therefore can only be defined using superoperators.

The absence of spatial phase factors in Eq. (8) indicates that the incoherent emission is isotropic and is independent of the wave vector of the incoming pulses. The single summation over molecules yields linear $\sim N$ scaling with the number of active molecules. The coherent signal (2) in contrast scales as $N(N-1)$. This signal is directional and propagates according to the phase matching condition $\mathbf{k}_s = \mathbf{k}_n$. The coherent and incoherent signals can always be distinguished by their $N(N-1)$ vs N scaling and directionality vs isotropic emission. A different type of size scaling exists in hyper-Rayleigh techniques. Consider a sample of M particles each composed of N molecules. Assuming coherent intraparticle and incoherent interparticle scattering, the signal will then scale as $MN(N-1)$ and will appear to be linearly scaling in the number of particles. N scaling can be similarly obtained if each molecule α is near some set of N' neighbor molecules β such that $|\mathbf{k}_s| \cdot |\mathbf{r}_\alpha - \mathbf{r}_\beta| \ll 1$; then it will emit in phase with this set of molecules, thus lending an overall factor of NN'. Incoherent sum frequency generation is an example of

a hyper-Rayleigh signal [38–40]. This signal scales linearly with the number of molecules, similar to the incoherent fluorescence.

Classically, spontaneous light emission from a nonstationary state is given by the Larmor formula (see Appendix D). All the necessary information is then contained in the charge density of the accelerating particle and the radiation power is related to the second-order time derivative of the macroscopic polarization. The classical derivation apparently applied even to a single molecule, and the result is then simply multiplied by the number of molecules. This yields linear N scaling. It follows from our analysis that the classical formula is valid only for the coherent signal from a mesoscopic volume and may not be applied to a single molecule. Light scattering from a single molecule is incoherent and provides new information about quantum pathways of matter. It may not be recast using the charge density alone.

To further evaluate the sum over molecules in Eqs. (2)–(11), we first consider small samples (compared to the optical wavelength) where retardation effects can be neglected. In this case both coherent and incoherent signals are independent of the direction of the incoming pulses. Straightforward analysis yields for the incoherent signal $\sum_\alpha R_\alpha^{-2} \sim N/R_c^2$, where R_c is the characteristic size of the sample. Similarly, since $|\mathbf{k}_n| \cdot |\mathbf{r}_\alpha - \mathbf{r}_\beta| \ll 1$, the coherent component yields $\sum_\alpha \sum_\beta (R_\alpha R_\beta)^{-1} \sim NN'/R_c^2$. Thus, both signals scale linearly with molecular density and inverse proportional to the square of the sample size. For extended samples, when retardation becomes important, the coherent signal yields a directional emission with N^2 scaling: $\sum_{\alpha,\beta} e^{i(\omega R_\alpha/c - \mathbf{k}_n \cdot \mathbf{R}_\alpha) - i(\omega' R_\beta/c - \mathbf{k}_n \cdot \mathbf{R}_\beta)} (R_\alpha R_\beta)^{-1} \simeq N(N-1)\delta(\omega/c - k_n)\delta(\omega'/c - k_n)$.

When retardation is neglected, the coherent signal (5) can be recast in the Larmor form. The most striking limitation is that this form may not be applied to the single-molecule case, as shown in Eq. (10); it requires pairs of molecules. The conventional classical derivations define the signal for a single molecule and then multiply it by the number of molecules. We showed that the N scaling can be realized in the coarse-grained system with mesoscopic grains via hyper-Rayleigh scattering where the short-range coherence makes the signal scale as N and not N^2.

III. LIGHT SCATTERING OFF A NONSTATIONARY STATE

We now calculate the incoherent and coherent signals in a multilevel system prepared in an arbitrary superposition state. In Sec. II, the evolution governed by $H'_-(t)$ and $H'(t)$ in Eqs. (3) and (9), respectively, caused by an arbitrary sequence of pulses which occurs prior to the last emission constitutes the preparation process that leaves the system in the superposition state. Here we ignore the details of the preparation (the shaded area in Fig. 2) and start our analysis after that time period where the system has been prepared in nonstationary superposition state: $\rho_{cc'}$ in Fig. 2(a) and two molecules in ρ_{cb} and $\rho_{bc'}$, respectively, in Fig. 2(b).

A. The coherent signal

We start with Eq. (3) and omitting the superscript α. For clarity we can recast the νth component of the polarization in

the form

$$P^{(\nu)}(t) = \mathrm{Tr}[V_\nu \rho(t)]. \tag{12}$$

After multiple interactions with incoming pulses the matter density matrix Fig. 2(b) is ρ_{cb}. We further define $\mu_{cb}^{(\nu)} \equiv \langle b|V_\nu|c\rangle$. We can then write

$$P^{(\nu)}(t) = \sum_{b,c} \rho_{cb}\mu_{bc}^{(\nu)} e^{-i\omega_{cb}t}. \tag{13}$$

Assuming that molecules α, β are identical and neglecting retardation we obtain the following compact form for the bare spectrogram:

$$
\begin{aligned}
&W_{B,\mathrm{coh}}(t',\omega')\\
&= N(N-1)\tilde{A}^2 \int_0^\infty d\tau\, e^{-i\omega'\tau}\, \ddot{P}(t'-\tau/2)\ddot{P}^*(t'+\tau/2),
\end{aligned}
\tag{14}
$$

where we have further averaged over the random dipole orientation $\sum_\nu P^{(\nu)}(t_1)P^{(\nu)*}(t_2) \simeq \frac{1}{3}P(t_1)P^*(t_2)$, yielding $\tilde{A} = A/\sqrt{3}$. Since $P(t)$ only depends on a single interaction with the signal mode, the coherent signal governed by the expectation value of the signal field is finite and the molecule returns to state $|b\rangle\langle b|$ at the end of the process. In the case of ideal time gating, we recover the Larmor formula

$$S_{\mathrm{coh}}(\bar{t}) = N(N-1)\frac{\tilde{A}^2}{2}|\ddot{P}(\bar{t})|^2, \tag{15}$$

where

$$\ddot{P}(t) = \sum_{b,c} \rho_{cb}\omega_{cb}^2 \mu_{bc}^{(\nu)} e^{-i\omega_{cb}\bar{t}}. \tag{16}$$

For purely frequency gating, we similarly get

$$S_{\mathrm{coh}}(\bar{\omega}) = N\tilde{A}^2 \sum_{b,c} \omega_{cb}^4 |\mu_{bc}|^2 |\rho_{cb}|^2 \delta(\bar{\omega}-\omega_{cb}). \tag{17}$$

B. The incoherent signal

To calculate the $\alpha = \beta$ terms in Eq. (A6) [see Fig. 2(a)] we must evaluate the following matter correlation function:

$$
\begin{aligned}
\langle \hat{V}_L(t_1')\hat{V}_R^\dagger(t_1)\rangle &= \mathrm{Tr}[\hat{V}^\dagger(t_1)\rho\hat{V}(t_1')]\\
&= \sum_{b,c,c'} \rho_{c,c'}\langle b|\hat{V}(t_1')|c\rangle\langle c'|\hat{V}^\dagger(t_1)|b\rangle\\
&= \sum_{b,c,c'} \rho_{cc'}\mu_{bc}\mu_{bc'}^* e^{-i\omega_{cb}t_1'} e^{i\omega_{c'b}t_1},
\end{aligned}
\tag{18}
$$

where the state of the system prior to the emission is given by the nonstationary density matrix element $\rho_{cc'}$ and the emission brings it to the population state $|b\rangle\langle b|$. Combining this with Eqs. (8) gives

$$
\begin{aligned}
W_{B,\mathrm{inc}}(t',\omega') &= \pi\tilde{A}^2 N \sum_{b,c,c'} \omega_{cb}^2 \omega_{c'b}^2 \mu_{bc}\mu_{bc'}^*\rho_{cc'}\\
&\quad \times e^{i(\omega_{c'b}-\omega_{cb})t'}\delta\left(\omega'-\frac{\omega_{cb}+\omega_{c'b}}{2}\right).
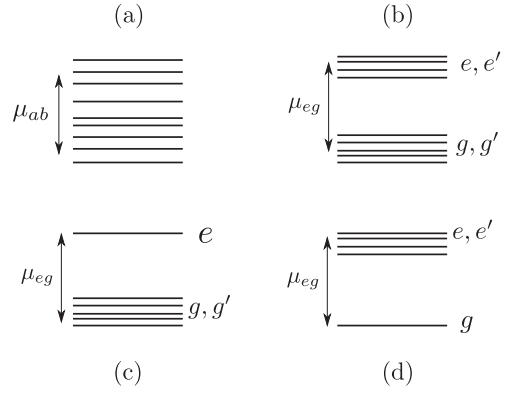\end{aligned}
\tag{19}
$$

FIG. 3. Various valence level schemes considered in this paper. (a) A general level scheme with arbitrary transition dipoles. (b) A two-band model with only interband transition dipole. (c) Two bands with a single excited state. (d) Two bands with a single ground state.

The incoherent bare spectrogram (19) may not be recast in the Larmor form [Eq. (14)]. The time-gated incoherent signal is

$$S_{\mathrm{inc}}(\bar{t}) = \frac{N\tilde{A}^2}{2}\sum_{b,c,c'} \omega_{cb}^2 \omega_{c'b}^2 \mu_{bc}\mu_{bc'}^*\rho_{cc'} e^{i(\omega_{c'b}-\omega_{cb})\bar{t}}. \tag{20}$$

The frequency-gated signal is

$$S_{\mathrm{inc}}(\bar{\omega}) = N\tilde{A}^2 \sum_{b,c} \omega_{cb}^4 \mu_{bc}^2 \rho_{cc}\delta(\bar{\omega}-\omega_{cb}). \tag{21}$$

In contrast with the coherent signal, we see that an excited-state population rather than a coherence in the relevant transitions is required to produce a signal. This is because all interactions are with a single molecule, and the radiation signal mode (initially in a vacuum state) must be brought to a population of one photon state to generate a signal.

We now apply our results to a level scheme composed of two manifolds of states with interband dipole elements as shown in Fig. 3(b), Eqs. (14)–(19), which gives

$$
\begin{aligned}
W_{B0,\mathrm{coh}}(t',\omega') &= \pi N\tilde{A}^2 \sum_{ee',gg'} \omega_{eg}^2 \omega_{e'g}^2 \mu_{ge}^*\mu_{g'e'}\rho_{ge}^*\rho_{g'e'}\\
&\quad \times e^{i(\omega_{eg}-\omega_{e'g'})t'}\delta\left(\omega'-\frac{\omega_{eg}+\omega_{e'g'}}{2}\right),
\end{aligned}
\tag{22}
$$

$$
\begin{aligned}
W_{B0,\mathrm{inc}}(t',\omega') &= \pi N\tilde{A}^2 \sum_{gee'} \omega_{eg}^2 \omega_{e'g}^2 \mu_{ge}^*\mu_{ge'}\rho_{ee'} e^{i(\omega_{eg}-\omega_{e'g})t'}\\
&\quad \times \delta\left(\omega'-\frac{\omega_{eg}+\omega_{e'g}}{2}\right),
\end{aligned}
\tag{23}
$$

where the subscript "0" signifies the two-band model. In the case of time and frequency gating, various transitions between ground and singly excited states become coupled. A time-gated measurement (4) yields

$$S_{0,\mathrm{coh}}(\bar{t}) = N\frac{\tilde{A}^2}{2}\left[\sum_{eg}\omega_{eg}^2 \mu_{ge}\rho_{ge} e^{-i\omega_{eg}\bar{t}}\right]^2, \tag{24}$$

$$S_{0,\mathrm{inc}}(\bar{t}) = N\frac{\tilde{A}^2}{2}\sum_g\sum_{e,e'}\omega_{eg}^2 \omega_{e'g}^2 \mu_{ge}\rho_{e'e} e^{i(\omega_{e'g}-\omega_{eg})\bar{t}}. \tag{25}$$

For an ideal frequency gating (6), the signal (22) and (23) reads

$$S_{0,\text{coh}}(\bar{\omega}) = N \tilde{A}^2 \sum_{eg} \omega_{eg}^4 |\mu_{ge}|^2 |\rho_{ge}|^2 \delta(\bar{\omega} - \omega_{eg}), \quad (26)$$

$$S_{0,\text{inc}}(\bar{\omega}) = N \tilde{A}^2 \sum_{eg} \omega_{eg}^4 |\mu_{ge}|^2 \rho_{ee} \delta(\bar{\omega} - \omega_{eg}). \quad (27)$$

Equations (26) and (27) are very similar, both given in the form of the Fermi golden rule for spectrally well-separated states. However, this is no longer the case for time-domain measurements. In Eq. (24), the initial and final states enter in the same way (the summations are fully interchangeable and all transitions are added at the amplitude level), while in Eq. (25), a trace is taken over final states after adding the amplitudes for the transitions to a given final state. The consequences of this difference are most readily seen by comparison of the two level schemes shown in Fig. 3. In case (c), there is a single excited state and a manifold of ground states. In case (d), the situation is reversed and there is a manifold of excited states and a single ground state. Both cases will generate a beating term in the coherent signal. In contrast, the incoherent signal (25) gives a beating term for case (d) but not for case (c). V- and Λ-type three-level models of atoms are commonly discussed in quantum optics [28,41]; these correspond to our cases (d) and (c), respectively. The total signal is $S = S_{\text{coh}} + S_{\text{inc}}$. S_{coh} only has beats for (d). The semiclassical approach only gives S_{coh}.

IV. DIFFERENCE-FREQUENCY-GENERATION VS FLUORESCENCE INDUCED BY A STIMULATED X-RAY RAMAN PROCESS

We have simulated these signals for cysteine, an amino acid which serves as an important structural unit in connecting different regions of proteins by disulfide bonds. The following excitation by a stimulated x-ray Raman process resonantly tuned to either the nitrogen, oxygen, or the sulfur K edges. The signal is given by the diagrams of Fig. 4 and involves six radiation-matter interactions. In this case the incoherent signal is SRIF and the coherent signal is DFG, as depicted in Fig. 4(c). An attosecond x-ray pulse excites the core transition to state f by absorbing a $\mathbf{k}_1$ photon which is then de-excited with a $-\mathbf{k}_2$ photon, leaving the system in a superposition of valence states g_1 and g_2 with amplitudes given by Eq. (A7) of Ref. [23]. This results in a weakly excited, pure-state g_3. We thus expect the incoherent and coherent signals to coincide for the $g_{1,2} \leftrightarrow g_0$ transition. The relevant diagrams are shown in Figs. 4(a) and 4(b). For a two-state model system prepared in a pure state, the state vector reads

$$|\psi_0\rangle = \kappa_g |g\rangle + \sum_e \kappa_e |e\rangle, \quad (28)$$

where expressions for κ_j, $j = e,g$ in Eq. (28) are given in Ref. [23]. In the limit of weak excitation most of the population is in the ground state $|\kappa_g|^2 \sim 1$ and $|\kappa_e|^2 \ll 1 \forall e$ (the excitation is perturbative). Thus Eq. (17) reads

$$S_{\text{coh}}(\bar{\omega}) = N \tilde{A}^2 \sum_{b,c} \omega_{cb}^4 |\mu_{bc}|^2 |\kappa_b|^2 |\kappa_c|^2 \delta(\bar{\omega} - \omega_{cb}). \quad (29)$$
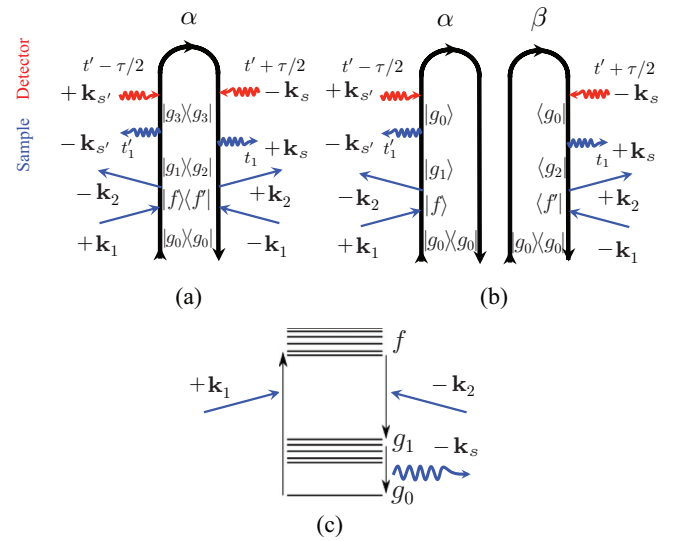

FIG. 4. (Color online) The stimulated x-ray Raman-induced NLS process. Straight arrows correspond to interactions with x-ray pulses, and wavy arrows represent spontaneous emission. (a) Loop diagram for the bare SRIF signal and (b) the bare coherent DFG signal. (c) The level scheme used for cysteine is composed of a ground state g_0 and 50 valence excited states g_1 with energies between $\sim$5.75 and $\sim$11.5 eV, and f are core excited states.

Since $|\kappa_e|^2 \ll 1$ and $|\kappa_g|^2 \sim 1$, the leading contribution yields

$$S_{\text{coh}}(\bar{\omega}) = N \tilde{A}^2 \sum_c \omega_{cg}^4 |\mu_{gc}|^2 |\kappa_c|^2 \delta(\bar{\omega} - \omega_{cg}), \quad (30)$$

where we assumed $b = g$. This is clearly a subset of the incoherent signal [Eq. (21)] which, under the assumption of a pure state, is given by

$$S_{\text{inc}}(\bar{\omega}) = N \tilde{A}^2 \sum_{b,c} \omega_{cb}^4 |\mu_{bc}|^2 |\kappa_b|^2 \delta(\bar{\omega} - \omega_{cb}). \quad (31)$$

Thus, for a weakly excited system in a pure state, the incoherent and coherent signals coincide for transitions from the excited states to the ground state. When the excited-state manifold bandwidth is smaller than the band gap, these transitions appear in the high-energy part of the emission spectra (see Sec. V). The intraband transitions within the excited-state manifold then appear in the red part of the spectra and only show up in the incoherent signal.

The optimized geometry was obtained with the quantum chemistry package Gaussian09 [42] at the B3LYP [32,43]/6-311G** level. Core excited states were calculated with restricted excitation window time-dependent density-functional theory (REW-TDDFT) [33] implemented in NWCHEM code [44]. Core and valence energy levels and transition dipole moments were calculated with a locally modified version of NWCHEM code at the CAM-B3LYP [45]/6-311G** level of theory and within the Tamm-Dancoff approximation [46]. Additional computational details are given in Ref. [24]. The calculated frequency-gated SRIF (21) and DFG (17) signals obtained by excitation of the nitrogen, oxygen, and sulfur K edges are shown in the top and bottom rows, respectively, of Fig. 5.
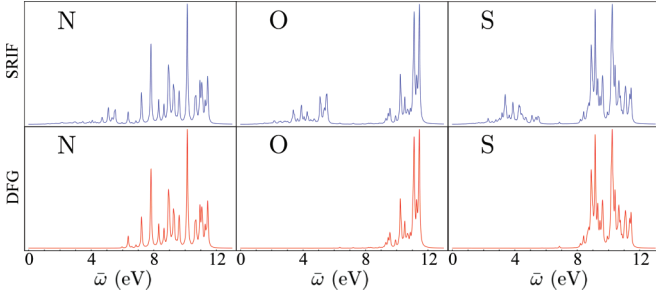
FIG. 5. (Color online) SRIF (top) and DFG (bottom) NLS signals of cysteine following stimulated Raman excitation by an x-ray pulse of width 14.2 eV and central frequency tuned to the nitrogen ($\sim$404.4 eV), oxygen ($\sim$532.2 eV), or sulfur ($\sim$2473.5 eV) K edges, as indicated. The two signals coincide for $g_{1,2} \leftrightarrow g_0$ transitions. Transitions between excited states $g_{1,2} \leftrightarrow g_3$, $\bar{\omega} < 5$ eV do not show up in the coherent signal. $\Gamma \sim 0.04$ eV is used for the gating bandwidth.

We first note that the SRIF and DFG signals coincide in the high-frequency regime. The lowest excited state has an energy $\sim$5.74 eV, while the excited-state manifold bandwidth is $\sim$5.70 eV. These high-energy transitions are from the various excited states to the ground state. The low-energy $\omega < 5$ eV features that only appear in the incoherent spectra represent transitions between excited states $g_{1,2} \leftrightarrow g_3$. The frequency-gated coherent and incoherent signals are very different. However, the corresponding time-gated signals shown in Fig. 6 are less distinct.

Figure 7 depicts the time- and frequency-gated spectrograms of the SRIF signal computed by Eq. (14) of Ref. [34] with Gaussian gating functions,

$$F_f(\omega, \bar{\omega}) = e^{-\frac{(\omega - \bar{\omega})^2}{2\sigma_\omega^2}}, \quad F_t(t, \bar{t}) = e^{-\frac{(t - \bar{t})^2}{2\sigma_T^2}}, \quad (32)$$
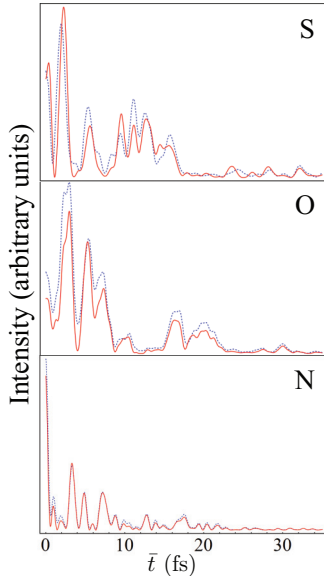

FIG. 6. (Color online) Time-resolved SRIF (solid red line) and DFG (dotted blue line signals) are compared for x-ray pulses resonant with S, O, and N in cysteine. $\Gamma \sim 0.04$ eV is used for the gating bandwidth.
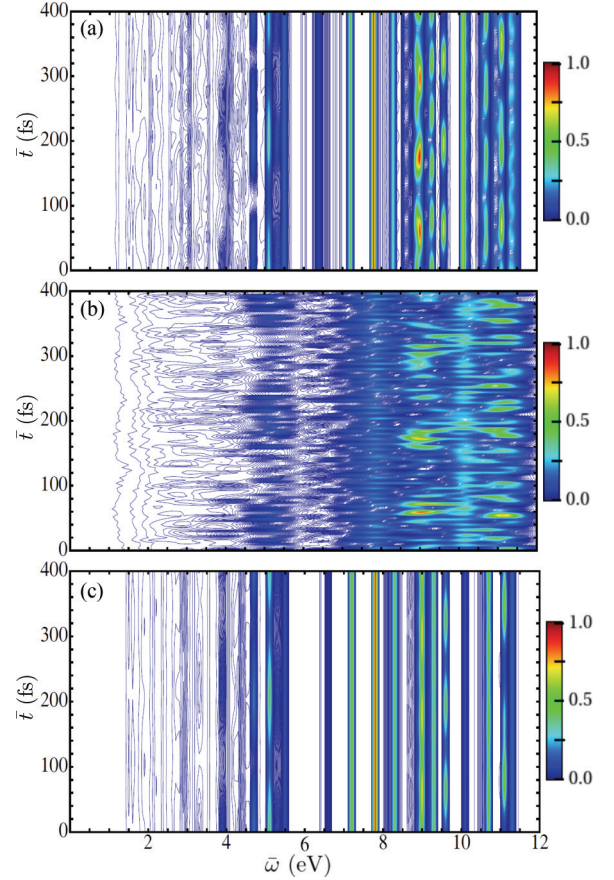

FIG. 7. (Color online) Time- and frequency-gated SRIF signals of cysteine [Eq. (1)]. The gating parameters in atomic units $\sigma_T = 1000$, $\sigma_\omega = 0.001$ (a), $\sigma_T = 100$, $\sigma_\omega = 0.01$ (b), and $\sigma_T = 2000$, $\sigma_\omega = 0.005$ (c). These permit all transitions within $\sim$0.054, 0.54, and 0.1 eV of each other to interfere, respectively. Top panel has optimal gating parameters and reveals both areas of low transition density (where the intensities are time independent) and areas of higher densities (where beats develop as a result of interference between transitions). Note the particularly prominent beating near 9 eV with an approximate period of 120 fs. The actual distance between these states is $\sim$0.0126 Ha, well within the allowed detection bandwidth. The middle panel has low-frequency resolution but rather high temporal resolution that results in a clear beating signal. The bottom panel has high spectral but low temporal resolution, which results in the suppression of formerly prominent beating at $\sim$9 eV. Further narrowing the frequency-domain gating widths eliminates it altogether.

where σ_ω and σ_T are the corresponding bandwidths of the frequency and time gates, respectively. These obey the Fourier uncertainty relation $\sigma_\omega \sigma_T \geqslant 1$. Some transitions in Fig. 7(a) do not vary with time while others beat. Beating occurs because of interference with nearby transitions and thus indicates a higher density of transitions. The beating period gives the interval between the interfering states a,b via $|\omega_{ab}| = \frac{2\pi}{T_{\text{beat}}}$. The gating parameters determine the maximum energy difference (and thus the minimum beating period) between interfering states via

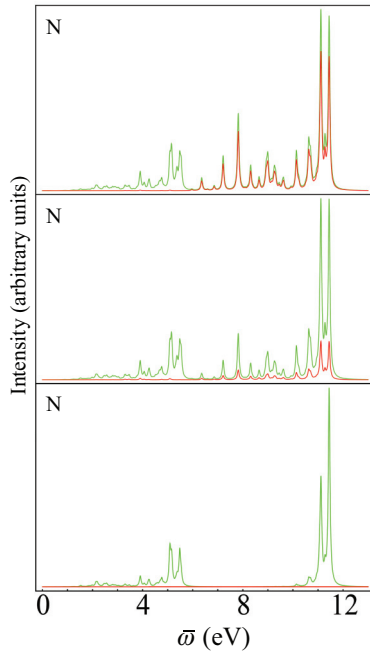$$\Delta = \sigma_\omega + \frac{1}{\sigma_T}, \quad (33)$$

FIG. 8. (Color online) Frequency-resolved SRIF, green (light gray) line, and DFG, red (dark gray) line, following a stimulated Raman excitation by two pulses of varying width. In all three panels, the first pulse is tuned to the transition from the bottom of the nitrogen core band to the ground state ($\sim$388 eV) and has a width of 1.36 eV. The second pulse is tuned to the transition from the bottom of the nitrogen core band to the top of the valence band ($\sim$374 eV). The second pulse is gradually broadened to allow for more valence excitations prior to the NLS $\sim$1.36 eV (bottom), $\sim$3 eV (middle), and $\sim$6 eV (top). $\Gamma \sim 0.04$ eV is used for the gating bandwidth.

where Δ is the maximum spacing between interfering states. Note that these resolutions always satisfy $\sigma_\omega \sigma_T \geqslant 1$ [35]. One can thus begin by applying a nearly pure frequency gating to eliminate interferences and then gradually widen the gating parameters in the frequency domain to reveal the density of transitions at various parts of the spectra. A clear demonstration is the prominently beating transitions with period $\sim$120 fs at $\sim$9 eV, which is visible (to varying degrees) in all three two-dimensional figures. An optimal balance for observing this interference is found in Fig. 7(a), in which the beating period (and thus the state separation) can be well approximated by visual inspection. In Fig. 7(b), Δ is so large that the interference of interest is masked by the myriad of other possible interferences, while in Fig. 7(c), Δ is small enough to almost entirely suppress the $\sim$9 eV beating. The coherent DFG signal coincides with SRIF in the regime $\bar{\omega} > 5$ eV and vanishes otherwise. Thus it is not plotted separately.

We note that the choice $\Gamma = 0.04$ eV in Figs. 5, 6, and 8 represents an experimental resolution. The lifetime of the valence states are of the order of nanoseconds and will give broadening $\Gamma \sim \mu$ eV. The detection parameters are chosen to capture the specific beating signal between various transitions that occur on much shorter time scale of tens of femtoseconds. The low quantum yield at short times poses a challenge for detection.

V. DISCUSSION

Thanks to the $\sim N^2$ vs $\sim N$ scaling, it is not hard to separate the coherent signal since it is directed and generally dominates the incoherent and hyper-Rayleigh coherent signals. However, it is not generally as simple to distinguish between the incoherent and hyper-Rayleigh contribution to the coherent signal, since both are roughly isotropic and $\sim N$ scaling. In our model of cysteine, the valence manifold bandwidth is slightly larger than the lowest valence excitation and so the incoherent and coherent signals can be easily distinguished in the frequency domain, as shown in Sec. IV.

When the valence-state manifold bandwidth is comparable to the band gap, both inter- and intraband transitions overlap spectrally and one needs to identify another procedure for separating the SRIF and DFG contributions. A single x-ray pulse cannot accomplish this goal, since any modification of its bandwidth will affect both the absorption and the emission profile. However, this can be achieved by using two x-ray pulses with wave vectors $\mathbf{k}_1$ and $-\mathbf{k}_2$ for the system preparation via stimulated Raman excitation. Both pulses must have narrow bandwidth compared to the g manifold in order to excite states selectively. The first pulse is tuned to the bottom of the core-excitation manifold. The second pulse is tuned to the transition from the bottom of the core-excitation manifold to the top of the valence band. This combination of pulse parameters can selectively excite populations and coherences of the high-energy valence states. Since the excitation is weak, the square of the ground and excited states coherences are comparable to the valence populations, but the coherences between valence states are lower order. Thus the coherences between valence states created by this two-pulse process do not contribute significantly to the signal. The overall signal will then be dominated by the incoherent contribution, in particular, the transitions from high-energy valence states to lower-energy valence states and the ground state. Increasing the bandwidth of pulse $-\mathbf{k}_2$ will result in the excitation of a larger number of valence states, which gives rise to a small coherent contribution as well as more transitions to appear in the incoherent spectra. Finally, as the second pulse is broadened so that it excites the entire valence band, the incoherent and coherent signals again overlap in the regime of transitions to the ground state. This behavior is illustrated in Fig. 8.

In summary, by working in the joint field-matter space we developed closed expressions for the NLS signal and show that may not be solely expressed in terms of the macroscopic polarization, as suggested by the semiclassical approach. We find an isotropic hyper-Rayleigh and directional coherent component that can be described by the Larmor formula and an incoherent component that governs the fluorescence. The microscopic calculation reveals interferences of the quantum matter pathways.

APPENDIX A: MICROSCOPIC CALCULATION OF SPONTANEOUS LIGHT EMISSION

Simultaneously, time- and frequency-gated spontaneous light emission signals may be described by the spectral and temporal overlap of a bare signal and a detector spectrogram [Eq. (1)]. The detector spectrogram W_D is an ordinary function of the time and frequency gating parameters, which are characterized by standard deviations of the time and frequency gating σ_T and σ_ω, respectively. The structure of W_D guarantees that these always satisfy the Fourier uncertainty $\sigma_\omega \sigma_T \geqslant 1$. The bare signal contains all of the relevant information about the molecules.

In order to maintain the bookkeeping of all interactions and develop a perturbative expansion for signals, we adopt superoperator notation. With each ordinary operator O we associate a pair of superoperators [31] "left" $\hat{O}_L X = O X$, "right" $\hat{O}_R X = X O$, and the combination $\hat{O}_- = \hat{O}_L - \hat{O}_R$. The bare spectrogram W_B in the gated photon counting signal (1) is given in terms of superoperators as

$$W_B(t',\omega') = \int_0^\infty d\tau e^{-i\omega'\tau} \langle \mathcal{T} \hat{\mathbf{E}}_R^\dagger(t'+\tau/2, \mathbf{r}_D) \hat{\mathbf{E}}_L$$
$$\times (t'-\tau/2, \mathbf{r}_D) e^{-\frac{i}{\hbar}\int_{-\infty}^\infty \hat{H}'_-(T)dT} \rangle. \quad (A1)$$

The positive frequency part of the electric field operator is given by

$$\hat{\mathbf{E}}(t,\mathbf{r}) = \sum_{\mathbf{k}_s,\mu} \left(\frac{2\pi\hbar\omega_s}{\Omega}\right)^{1/2} \epsilon^{(\mu)}(\mathbf{k}_s) \hat{a}_{\mathbf{k}_s} e^{-i\omega_s t + i\mathbf{k}_s\cdot\mathbf{r}}, \quad (A2)$$

where $\epsilon^{(\mu)}(\mathbf{k})$ is the unit electric polarization vector of mode $(\mathbf{k}_s,\mu)$, μ being the index of polarization, $\omega_s = c|\mathbf{k}_s|$, c is the speed of light, and Ω is quantization volume. The polarization degrees of freedom are necessary to restrict the density of radiation modes and recover the λ^{-4} dependence typical for Rayleigh scattering. The Hamiltonian superoperator in the interaction picture under the rotating-wave approximation (RWA) is given by

$$\hat{H}'_q(t) = \int d\mathbf{r} \hat{\mathbf{E}}_q^\dagger(t,\mathbf{r}) \hat{\mathbf{V}}_q(t,\mathbf{r}) + \text{H.c.}, \quad q = L, R, \quad (A3)$$

where $\mathbf{V}(t,\mathbf{r}) = \sum_\alpha \mathbf{V}^\alpha(t) \delta(\mathbf{r} - \mathbf{r}_\alpha)$ is a matter operator representing the lowering (exciton annihilation) part of the dipole coupling and α runs over molecules in the sample located at $\mathbf{r}_\alpha$, $\mathbf{r}_\beta$. The operator $\mathcal{T}$ maintains positive time ordering of superoperators and is a key bookkeeping device. It is defined as follows:

$$\mathcal{T} \hat{E}_q(t_1) \hat{E}_{q'}(t_2) = \theta(t_1 - t_2) \hat{E}_q(t_1) \hat{E}_{q'}(t_2)$$
$$+ \theta(t_2 - t_1) \hat{E}_{q'}(t_2) \hat{E}_q(t_1), \quad (A4)$$

where $\theta(t)$ is the Heaviside step function. Note that the interaction Hamiltonian (A3) corresponds to the interaction of the matter with the spontaneously emitted photon between two electronic states. This energy is in VUV range and is not related to the preparation of the system that involves an x-ray Raman process with high-energy photons. Therefore the dipole approximation for field-matter interaction is justified.

We shall calculate the time-dependent bare signal (A1) for a collection of molecules α, β in the interaction picture. We consider a signal governed by the spatial phase factor $e^{i\mathbf{k}_n\cdot\mathbf{r}}$, where $\mathbf{k}_n$ is a combination of incoming wave vectors characteristic to the desired signal. This phase factor represents a paraxial approximation, such that multiple frequency components propagate with the same wave vector. The bare signal is represented by the closed-path time-loop diagram shown in Figs. 2(a) and 2(b). We first expand the time-ordered exponent in Eq. (A1) to second order—one interaction with the bra and one with the ket—and factorize the detected field and matter correlation functions as follows:

$$\frac{1}{\hbar^2} \sum_{\alpha,\beta}^N \sum_{\nu,\nu'} \int_{-\infty}^{t'+\tau/2} dt_1 \int_{-\infty}^{t'-\tau/2} dt_1' \langle \mathcal{T} \hat{V}_{\nu L}^\alpha(t_1') \hat{V}_{\nu' R}^{\beta\dagger}(t_1) \rangle \langle \mathcal{T} \hat{E}_{\mu R}^{(s)\dagger}(t'+\tau/2, \mathbf{r}_D) \hat{E}_{\mu L}^{(s')}(t'-\tau/2, \mathbf{r}_D) \hat{E}_{\nu L}^{(s')\dagger}(t_1', \mathbf{r}_\alpha) \hat{E}_{\nu' R}^{(s)}(t_1, \mathbf{r}_\beta) \rangle. \quad (A5)$$

Since $\hat{E}^{(s)}$ is initially in the vacuum state, the field correlation function factorizes using (A2) and the bare signal (A1) is given by

$$W_B(t',\omega') = \left(\frac{2\pi}{\Omega}\right)^2 \sum_{\mathbf{k}_s,\mathbf{k}_{s'}} \int_0^\infty d\tau e^{-i\omega'\tau} \int_{-\infty}^{t'+\tau/2} dt_1 \int_{-\infty}^{t'-\tau/2} dt_1' \omega_s \omega_{s'} e^{i\omega_s(t'+\tau/2-t_1) - i\omega_{s'}(t'-\tau/2-t_1')} \sum_{\alpha,\beta}^N e^{i(\mathbf{k}_s-\mathbf{k}_n)\cdot\mathbf{R}_\beta - i(\mathbf{k}_{s'}-\mathbf{k}_n)\cdot\mathbf{R}_\alpha}$$
$$\times \sum_{\mu,\nu,\nu'} \epsilon^{(\nu)}(\mathbf{k}_s) \epsilon^{(\mu)}(\mathbf{k}_s) \epsilon^{(\nu')}(\mathbf{k}_{s'}) \epsilon^{(\mu)}(\mathbf{k}_{s'}) \langle \mathcal{T} \hat{V}_{\nu L}^\alpha(t_1') \hat{V}_{\nu' R}^{\beta\dagger}(t_1) e^{-\frac{i}{\hbar}\int_{-\infty}^\infty \hat{H}'_-(T)dT} \rangle, \quad (A6)$$

where $\mathbf{R}_\alpha = \mathbf{r}_\alpha - \mathbf{r}_D$ and $\mathbf{r}_D$ is the position of the detector. Equation (A6) explicitly contains multiple pairs of radiation modes $\mathbf{k}_s$ and $\mathbf{k}_{s'}$, and acts in the joint field plus matter space. It takes into account all field-matter interactions that lead to the emission of the detected field modes.

APPENDIX B: SUPEROPERATOR REPRESENTATION OF COHERENT AND INCOHERENT SIGNALS

For the single-molecule (incoherent) signal $\mathbf{r}_\alpha = \mathbf{r}_\beta$, and thus the signal reads

$$W_{B\text{inc}}(t',\omega') = \left(\frac{2\pi}{\Omega}\right)^2 \sum_{\mathbf{k}_s,\mathbf{k}_{s'}} \int_0^\infty d\tau e^{-i\omega'\tau} \sum_\alpha^N e^{i(\mathbf{k}_s-\mathbf{k}_{s'})\cdot\mathbf{R}_\alpha} \int_{-\infty}^{t'+\tau/2} dt_1 \int_{-\infty}^{t'-\tau/2} dt_1' \omega_s \omega_{s'}' e^{i\omega_s(t'+\tau/2-t_1) - i\omega_{s'}'(t'-\tau/2-t_1')}$$
$$\times \sum_{\mu,\nu,\nu'} \epsilon^{(\nu)}(\mathbf{k}_s) \epsilon^{(\mu)}(\mathbf{k}_s) \epsilon^{(\nu')}(\mathbf{k}_{s'}) \epsilon^{(\mu)}(\mathbf{k}_{s'}) \langle \mathcal{T} \hat{V}_{\nu L}(t_1') \hat{V}_{\nu' R}^\dagger(t_1) e^{-\frac{i}{\hbar}\int_{-\infty}^\infty \hat{H}'_-(T)dT} \rangle_\alpha. \quad (B1)$$

In the absence of dissipation (unitary evolution) we can further factorize the matter correlation function as

$$\langle \mathcal{T} \hat{V}_{\nu L}(t_1') \hat{V}_{\nu' R}^{\dagger}(t_1) \rangle = \sum_{a,b} \rho_{aa} \langle\langle aa| \hat{V}_{\nu' R}^{\dagger}(t_1)|ab\rangle\rangle \langle\langle ba| \hat{V}_{\nu L}(t_1')|aa\rangle\rangle$$

$$= \sum_{a,b} \rho_{aa} \left\langle \langle b(t'+\tau/2)a| \hat{V}_{\nu L}(t_1') \mathcal{T}_{+} \exp\left[-\frac{i}{\hbar} \int_{-\infty}^{t_1'} \hat{H}_L'(T) dT\right] |aa\rangle \right\rangle \left\langle \langle aa| \hat{V}_{\nu' R}^{\dagger}(t_1) \mathcal{T}_{-} \right.$$

$$\left. \times \exp\left[\frac{i}{\hbar} \int_{-\infty}^{t_1} \hat{H}_R'(T) dT\right] |b(t'+\tau/2)a\rangle \right\rangle, \tag{B2}$$

where we denote $\langle\langle ba| \hat{O}|aa\rangle\rangle \equiv \mathrm{Tr}[|a\rangle\langle b| \hat{O}|a\rangle\langle a|]$ and b is the final state of the system. We assume that system is initially in the pure state a described by equilibrium density matrix ρ_{aa}. We next define the transition amplitude:

$$\tilde{T}_{ba}^{(\alpha,\mu)}(t) = -i \sum_{\mathbf{k}_s,\nu} \epsilon^{(\nu)}(\mathbf{k}_s) \epsilon^{(\mu)}(\mathbf{k}_s) \frac{2\pi\omega_s}{\Omega} \int_{-\infty}^{t} dt_1' e^{-i\omega_s(t-t_1')-i\omega_{ab}t-i(\mathbf{k}_s-\mathbf{k}_{\{n\}})\cdot\mathbf{R}_\alpha} \left\langle \langle b(t)a| \hat{V}_{\nu L}(t_1') \mathcal{T} \exp\left(-\frac{i}{\hbar} \int_{-\infty}^{t_1'} \hat{H}_L'(T) dT\right) |aa\rangle \right\rangle_\alpha. \tag{B3}$$

Since all interactions are from the left (L), we can also write the transition amplitude using ordinary operators in Hilbert space,

$$\tilde{T}_{ba}^{(\alpha,\mu)}(t) = -i \sum_{\mathbf{k}_s,\nu} \epsilon^{(\nu)}(\mathbf{k}_s) \epsilon^{(\mu)}(\mathbf{k}_s) \frac{2\pi\omega_s}{\Omega} \int_{-\infty}^{t} dt_1' e^{-i\omega_s(t-t_1')-i\omega_{ab}t-i(\mathbf{k}_s-\mathbf{k}_{\{n\}})\cdot\mathbf{R}_\alpha} \langle b(t)| V_\nu(t_1') \mathcal{T} \exp\left(-\frac{i}{\hbar} \int_{-\infty}^{t_1'} H'(T) dT\right) |a\rangle_\alpha. \tag{B4}$$

This gives for the bare signal (B1),

$$W_{B\mathrm{inc}}(t',\omega') = \sum_{a,b,\mu} \sum_{\alpha=1}^{N} \rho_{aa} \int_{0}^{\infty} d\tau e^{-i\omega'\tau} \tilde{T}_{ba}^{(\alpha,\mu)}(t'-\tau/2) \tilde{T}_{ab}^{(\alpha,\mu)*}(t'+\tau/2). \tag{B5}$$

In the limit of pure time-resolved measurement (4), signal (B5) transforms into

$$W_{B\mathrm{inc}}(\bar{t}) = \sum_{a,b,\mu} \sum_{\alpha=1}^{N} \rho_{aa} \left| \tilde{T}_{ba}^{(\alpha,\mu)}(\bar{t}) \right|^2. \tag{B6}$$

Similarly, the pure frequency-resolved signal (6) signal (B5) yields

$$W_{B\mathrm{inc}}(\bar{\omega}) = \sum_{a,b,\mu} \sum_{\alpha=1}^{N} \rho_{aa} \left| \tilde{T}_{ba}^{(\alpha,\mu)}(\bar{\omega}) \right|^2, \tag{B7}$$

where $\tilde{T}_{ba}^{(\alpha,\mu)}(\omega) = \int_{-\infty}^{\infty} dt \, \tilde{T}_{ba}^{(\alpha,\mu)}(t) e^{i\omega t}$. The spatial phase factors in Eq. (A6) indicate that the incoherent emission occurs in all directions and is independent of the wave vector of the incoming pulses as expected. A single summation over the molecule yields the linear scaling with respect to the number of molecules.

We now turn to coherent emission contribution of $\alpha \neq \beta$. Since interactions with different molecules are not time ordered, we may factorize the matter correlation in Eq. (A6) $\langle \mathcal{T} \hat{V}_L^\alpha(t_1') \hat{V}_R^{\beta\dagger}(t_1) \rangle \rightarrow \langle \hat{V}_L^\alpha(t_1') \rangle \langle \hat{V}_R^{\beta\dagger}(t_1) \rangle$. Thus the two-molecule (coherent) signal can be separated into a long-range and a short-range component (as described in Ref. [47]). Using Eqs. (B2) and (B3) the coherent part of the signal (A6) reads

$$W_{B\mathrm{coh}}(t',\omega') = \sum_{\mu} \sum_{\alpha=1}^{N} \sum_{\beta=1}^{N-1} \int_{0}^{\infty} d\tau e^{-i\omega'\tau} \tilde{P}^{(\alpha,\mu)}(t'-\tau/2) \tilde{P}^{(\beta,\mu)}(t'+\tau/2), \tag{B8}$$

where

$$\tilde{P}^{(\alpha,\mu)}(t) = -i \sum_{\mathbf{k}_s,\nu} \epsilon^{(\nu)}(\mathbf{k}_s) \epsilon^{(\mu)}(\mathbf{k}_s) \frac{2\pi\omega_s}{\Omega} \int_{-\infty}^{t} dt_1' e^{-i\omega_s(t-t_1')-i\omega_{ab}t-i(\mathbf{k}_s-\mathbf{k}_{\{n\}})\cdot\mathbf{R}_\alpha}$$

$$\times \sum_{a,b} \rho_{aa} \left\langle \langle bb| \hat{V}_{\nu L}(t_1') \mathcal{T} \exp\left(-\frac{i}{\hbar} \int_{-\infty}^{t_1'} \hat{H}_L'(T) dT\right) |aa\rangle \right\rangle_\alpha. \tag{B9}$$

Here ρ_{aa} represents the initial equilibrium density matrix. Note that in contrast with Eq. (B3), which represents the transition amplitude and thus can be recast in Hilbert space, (B9) is related to polarization and therefore can be written in Liouville space only. In the limit of pure time-resolved measurement (4) signal (B8) transforms into

$$W_{B\mathrm{coh}}(\bar{t}) = \sum_{\mu} \sum_{\alpha=1}^{N} \sum_{\beta=1}^{N-1} \tilde{P}^{(\alpha,\mu)}(\bar{t}) \tilde{P}^{(\beta,\mu)}(\bar{t}). \tag{B10}$$

Similarly, the pure frequency-resolved signal (6) signal (B8) yields

$$W_{B\text{coh}}(\bar{\omega}) = \sum_{\mu} \sum_{\alpha=1}^{N} \sum_{\beta=1}^{N-1} \tilde{P}^{(\alpha,\mu)}(\bar{\omega}) \tilde{P}^{(\beta,\mu)}(\bar{\omega}). \quad \text{(B11)}$$

APPENDIX C: MICROSCOPIC DERIVATION OF THE LARMOR FORMULA

In order to calculate the signal (A6), we start with amplitude expression (B3). We first evaluate the summation over the modes. In the continuum limit

$$\frac{1}{\Omega} \sum_{\mathbf{k}_s} = \frac{1}{(2\pi)^3} \int d\mathbf{k}_s. \quad \text{(C1)}$$

Recalling that $\hat{\mathbf{k}}_s$ and polarization vectors $\epsilon^{(\nu)}(\mathbf{k}_s)$, $\nu = 1,2$ form a set of mutually perpendicular unit vectors, it follows that

$$\epsilon^{(\nu)}(\mathbf{k}_s) \epsilon^{(\mu)}(\mathbf{k}_s) = \delta_{\mu\nu} - \hat{k}_\mu \hat{k}_\nu. \quad \text{(C2)}$$

We further evaluate the momentum integral using $d\mathbf{k}_s = k_s^2 dk_s d\Omega$. The angular integration yields

$$\frac{1}{4\pi} \int d\Omega (\delta_{\mu\nu} - \hat{k}_\mu \hat{k}_\nu) e^{i\mathbf{k}_s \cdot \mathbf{R}}$$
$$= \frac{1}{k_s^3} (-\nabla^2 \delta_{\mu\nu} + \nabla_\mu \cdot \nabla_\nu) \frac{\sin(k_s R)}{R}. \quad \text{(C3)}$$

Equation (B3) then yields

$$\tilde{T}_{ba}^{(\alpha,\mu)}(t) = \frac{e^{i\mathbf{k}_n \cdot \mathbf{R}_\alpha}}{\pi} \sum_{\nu} \int \frac{d\omega}{2\pi} T_{ba}^{(\alpha,\nu)}(\omega) e^{-i\omega t}$$
$$\times \int d\omega_s (-\nabla^2 \delta_{\mu\nu} + \nabla_\mu \cdot \nabla_\nu) \frac{\sin(\omega_s R_\alpha/c)}{R_\alpha}$$
$$\times \frac{1}{\omega - \omega_s + i\epsilon}, \quad \text{(C4)}$$

where we introduced a matter transition amplitude $T_{ba}(\omega)$ that connects the initial state a with final state b: $T_{ba}^{(\alpha,\nu)}(\omega) = \int_{-\infty}^{\infty} dt e^{i\omega t} T_{ba}^{(\alpha,\nu)}(t)$ and $T_{ba}^{(\alpha,\nu)}(t)$ is given by Eq. (9). We then note that

$$\int d\omega_s \frac{\sin(\omega_s R_\alpha/c)}{\omega_s - \omega - i\epsilon} = \pi e^{i\omega R_\alpha/c}. \quad \text{(C5)}$$

Taking into account that [36]

$$(-\nabla^2 \delta_{\mu\nu} + \nabla_\mu \cdot \nabla_\nu) \frac{e^{ikR}}{R}$$
$$= \frac{1}{R^3} [(\delta_{\mu\nu} - 3\hat{R}_\mu \hat{R}_\nu)(ikR - 1) + (\delta_{\mu\nu} - \hat{R}_\mu \hat{R}_\nu) k^2 R^2] e^{ikR} \quad \text{(C6)}$$

and assuming the random orientation of the molecules, $\hat{R}_\mu \hat{R}_\nu = \frac{1}{3}\delta_{\mu\nu}$, we obtain

$$\tilde{T}_{ba}^{(\alpha,\mu)}(t) = -\frac{2}{3c^2} \frac{e^{i\mathbf{k}_n \cdot \mathbf{R}_\alpha}}{R_\alpha} \partial_t^2 T_{ba}^{(\mu,\alpha)}(t - R_\alpha/c). \quad \text{(C7)}$$

Taking into account (B5) we therefore obtain (8). Similarly, we derive for a coherent signal

$$\tilde{P}^{(\alpha,\mu)}(t) = -\frac{2}{3c^2} \frac{e^{i\mathbf{k}_n \cdot \mathbf{R}_\alpha}}{R_\alpha} \partial_t^2 P^{(\mu,\alpha)}(t - R_\alpha/c). \quad \text{(C8)}$$

Thus coherent signal Eq. (B8) can be recast in the form of (2).

APPENDIX D: SEMICLASSICAL THEORY OF EMISSION DETECTION FROM A RADIATING DIPOLE

According to classical electrodynamics, the electric field obeys the usual homogeneous wave equation derived from Maxwell equations:

$$\nabla \times \nabla \times \mathbf{E}(\mathbf{r},t) - \frac{1}{c^2} \frac{\partial^2 \mathbf{E}(\mathbf{r},t)}{\partial t^2} = \frac{1}{\epsilon_0 c^2} \frac{\partial^2 \tilde{\mathbf{P}}(\mathbf{r},t)}{\partial t^2}. \quad \text{(D1)}$$

Here $\tilde{\mathbf{P}}$ is the macroscopic polarization and ϵ_0 is the vacuum permittivity. Since Eq. (D1) is linear, it applies also for a quantum field, where the electric field $\mathbf{E}$ and $\tilde{\mathbf{P}}$ become operators. Restricting ourselves to the transverse part in far field $E = E_\perp$, this equation can be recast in the frequency domain as

$$\nabla^2 E(\mathbf{r},\omega) - \frac{\omega^2}{c^2} E(\mathbf{r},\omega) = \frac{\omega^2}{\epsilon_0 c^2} \tilde{P}(\mathbf{r},\omega). \quad \text{(D2)}$$

The Green's function solution of Eq. (D2) in infinite space for a single-point dipole molecule at $\mathbf{r} = 0$ is

$$E(\mathbf{r},\omega) = -\frac{1}{\epsilon_0 c^2} \omega^2 \frac{e^{ik_0|\mathbf{r}|}}{4\pi |\mathbf{r}|} \tilde{P}(0,\omega), \quad \text{(D3)}$$

where $k_0 = \omega/c$. The latter can be recast in the time domain

$$E(\mathbf{r},t) = \frac{1}{\epsilon_0 c^2} \frac{1}{4\pi |\mathbf{r}|} \partial_t^2 \tilde{P}(0,t - |\mathbf{r}|/c). \quad \text{(D4)}$$

Neglecting retardation effects, the electric field entering the detector at position r_G is given by

$$E(r_G,t) = B \ddot{P}(t), \quad \text{(D5)}$$

where $B = (4\pi \epsilon_0 c^2 |r_G|)^{-1}$ and $P(t) \equiv \tilde{P}(0,t)$. We thus recover the Larmor formula for the time-resolved intensity of the signal,

$$S(t) = B^2 |\ddot{P}(t)|^2. \quad \text{(D6)}$$

Generally the signal will be affected by the detector geometry, depending if an angle is used with a lens or if it enters in parallel. These details will affect the prefactor B and are not considered here. The bare signal can be finally calculated as

$$W_B(t',\omega') = B^2 \int_0^\infty d\tau e^{-i\omega' \tau} \ddot{P}^*(t' + \tau/2) \ddot{P}(t' - \tau/2). \quad \text{(D7)}$$

[1] J. Ullrich, A. Rudenko, and R. Moshammer, Annu. Rev. Phys. Chem. **63**, 635 (2012).

[2] L. Gallmann, C. Cirelli, and U. Keller, Annu. Rev. Phys. Chem. **63**, 447 (2012).

[3] P. Emma *et al.*, Nat. Photon. **4**, 641 (2010).

[4] H. Kapteyn, O. Cohen, I. Christov, and M. Murnane, Science **317**, 775 (2007).

[5] F. Krausz and M. Ivanov, Rev. Mod. Phys. **81**, 163 (2009).

[6] H. J. Wörner and P. B. Corkum, in *Handbook of High-Resolution Spectroscopy* (John Wiley & Sons, Ltd., New York, 2011).

[7] M. Hentschel, R. Kienberger, C. Spielmann, G. A. Reider, N. Milosevic, T. Brabec, P. Corkum, U. Heinzmann, M. Drescher, and F. Krausz, Nature (London) **414**, 509 (2001).

[8] T. Popmintchev, M. Chen, D. Popmintchev, P. Arpin, S. Brown, S. Ališauskas, G. Andriukaitis, T. Balčiunas, O. D. Mücke, A. Pugzlys, A. Baltuška, B. Shim, S. E. Schrauth, A. Gaeta, C. Hernández-García, L. Plaja, A. Becker, A. Jaron-Becker, M. M. Murnane, and H. C. Kapteyn, Science **336**, 1287 (2012).

[9] A. Zholents and G. Penn, Nucl. Instrum. Methods Phys. Res., Sect. A **612**, 254 (2010).

[10] S. Mukamel, D. Healion, Y. Zhang, and J. D. Biggs, Annu. Rev. Phys. Chem. **64**, 101 (2013).

[11] L. J. P. Ament, M. van Veenendaal, T. P. Devereaux, J. P. Hill, and J. van den Brink, Rev. Mod. Phys. **83**, 705 (2011).

[12] N. Rohringer and R. Santra, Phys. Rev. A **79**, 053402 (2009).

[13] A. I. Kuleff and L. S. Cederbaum, Phys. Rev. Lett. **106**, 053001 (2011).

[14] F. de Groot and A. Kotani, *Core Level Spectroscopy of Solids*, 1st ed. (CRC Press, Boca Raton, FL, 2008).

[15] G. Dixit, O. Vendrell, and R. Santra, Proc. Natl. Acad. Sci. USA **109**, 11636 (2012).

[16] J. Breidbach and L. S. Cederbaum, Phys. Rev. Lett. **94**, 033901 (2005).

[17] B. Adams, *Nonlinear Optics, Quantum Optics, and Ultrafast Phenomena with X-Rays*, 1st ed. (Springer, Berlin, 2003).

[18] P. M. Eisenberger and S. L. McCall, Phys. Rev. A **3**, 1145 (1971).

[19] Y. Yoda, T. Suzuki, X. Zhang, K. Hirano, and S. Kikuta, J. Synchrotron Radiat. **5**, 980 (1998).

[20] B. Adams, P. Fernandez, W. K. Lee, G. Materlik, D. M. Mills, and D. V. Novikov, J. Synchrotron Radiat. **7**, 81 (2000).

[21] A. Nazarkin, S. Podorov, I. Uschmann, E. Förster, and R. Sauerbrey, Phys. Rev. A **67**, 041804 (2003).

[22] Y. Bannett and I. Freund, Phys. Rev. Lett. **49**, 539 (1982).

[23] J. D. Biggs, Y. Zhang, D. Healion, and S. Mukamel, J. Chem. Phys. **136**, 174117 (2012).

[24] Y. Zhang, J. D. Biggs, D. Healion, N. Govind, and S. Mukamel, J. Chem. Phys. **137**, 194306 (2012).

[25] T. Popmintchev, M. Chen, P. Arpin, M. M. Murnane, and H. C. Kapteyn, Nat. Photon. **4**, 822 (2010).

[26] F. Gel'mukhanov and H. Ågren, Phys. Rep. **312**, 87 (1999).

[27] U. Harbola and S. Mukamel, Phys. Rev. B **79**, 085108 (2009).

[28] M. O. Scully and M. S. Zubairy, *Quantum Optics* (Cambridge University Press, Cambridge, UK, 1997).

[29] J. D. Jackson, *Classical Electrodynamics*, 3rd ed. (Wiley, New York, 1998).

[30] S. Tanaka, V. Chernyak, and S. Mukamel, Phys. Rev. A **63**, 063405 (2001).

[31] U. Harbola and S. Mukamel, Phys. Rep. **465**, 191 (2008).

[32] P. Stephens, F. Devlin, C. Chabalowski, and M. Frisch, J. Phys. Chem. **98**, 11623 (1994).

[33] K. Lopata, B. E. V. Kuiken, M. Khalil, and N. Govind, J. Chem. Theory Comput. **8**, 3284 (2012).

[34] K. E. Dorfman and S. Mukamel, Phys. Rev. A **86**, 013810 (2012).

[35] H. Stolz, *Time-Resolved Light Scattering from Excitons* (Springer-Verlag, Berlin, 1994).

[36] A. Salam, *Molecular Quantum Electrodynamics: Long Range Intermolecular Interactions* (Wiley, Hoboken, NJ, 2010).

[37] S. Mukamel and S. Rahav, Adv. At. Mol. Opt. Phys. **59**, 223 (2010).

[38] R. W. Terhune, P. D. Maker, and C. M. Savage, Phys. Rev. Lett. **14**, 681 (1965).

[39] K. Clays and A. Persoons, Phys. Rev. Lett. **66**, 2980 (1991).

[40] K. Clays, E. Hendrickx, M. Triest, T. Verbiest, A. Persoons, C. Dehu, and J.-L. Brdas, Science **262**, 1419 (1993).

[41] K. E. Dorfman, P. K. Jha, and S. Das, Phys. Rev. A **84**, 053803 (2011).

[42] M. J. Frisch *et al.*, "Gaussian 09" (Gaussian, Inc., Wallingford, CT, 2009).

[43] A. D. Becke, J. Chem. Phys. **98**, 5648 (1993).

[44] M. Valiev, E. Bylaska, N. Govind, K. Kowalski, T. Straatsma, H. van Dam, D. Wang, J. Nieplocha, E. Apra, T. Windus, and W. de Jong, Comput. Phys. Commun. **181**, 1477 (2010).

[45] T. Yanai, D. P. Tew, and N. C. Handy, Chem. Phys. Lett. **393**, 51 (2004).

[46] S. Hirata and M. Head-Gordon, Chem. Phys. Lett. **314**, 291 (1999).

[47] O. Roslyak and S. Mukamel, "A unified quantum field description of spontaneous and stimulated nonlinear wave mixing and hyper-rayleigh scattering," Lectures of Virtual University, Max-Born Institute, EVU Lecture Notes (2010).